Identifying Z_{DR} Columns in Radar Data with the Hotspot Technique🖉

JOHN KRAUSE[a,b] AND VINZENT KLAUS[c]

[a] *Cooperative Institute for Severe and High-Impact Weather Research and Operations, University of Oklahoma, Norman, Oklahoma*
[b] *NOAA/OAR/National Severe Storms Laboratory, Norman, Oklahoma*
[c] *Institute of Meteorology and Climatology, Department of Water, Atmosphere and Environment,
University of Natural Resources and Life Sciences, Vienna, Austria*

ABSTRACT: A novel differential reflectivity (Z_{DR}) column detection method, the hotspot technique, has been developed. Utilizing constant altitude plan projection indicators (CAPPI) of Z_{DR}, reflectivity, and a proxy for circular depolarization ratio at the height of the $-10°C$ isotherm, the method identifies the location of the base of the Z_{DR} column rather than the entire Z_{DR} column depth. The new method is compared to two other existing Z_{DR} column detection methods and shown to be an improvement in regions where there is a Z_{DR} bias.

SIGNIFICANCE STATEMENT: Thunderstorm updrafts are the area of a storm where precipitation grows, electrification is initiated, and tornadoes may form. Therefore, accurate detection and quantification of updraft properties using weather radar data is of great importance for assessing a storm's damage potential in real time. Current methods to automatically detect updraft areas, however, are error-prone due to common deficiencies in radar measurements. We present a novel algorithmic approach to identify storm updrafts that eliminates some of the known shortcomings of existing methods. In the future, our method could be used to develop new hail detection algorithms, or to improve short-term weather forecasting models.

1. Introduction

High Z_{DR} (e.g., >1 dB) values found above the environmental freezing level (0°C) can be created by, among other things, large raindrops and wet hail suspended in strong convective updrafts (e.g., Kumjian et al. 2014; Snyder et al. 2015). Convective storm updrafts can also sort liquid water drops by size, suspending large drops [e.g., $Z_{DR} > 1$ dB corresponding to ≥3-mm raindrops Ryzhkov and Zrnić (2019)] while ejecting smaller drops (e.g., $Z_{DR} < 1$ dB). Depending on the vertical velocity of the updraft, the region of high Z_{DR} can extend several kilometers above the environmental freezing level. This polarimetric signature of vertically correlated high Z_{DR} values found above the melting layer within convective storms is called the Z_{DR} column. Z_{DR} columns in polarimetric radar data have been used to study the initiation and development of convective cells in observational studies and in convective storm modeling experiments (e.g., Kumjian et al. 2014; Carlin et al. 2017; Snyder et al. 2017a,b). Used as a proxy for the updraft of the convective storm, a Z_{DR} column's magnitude, location, cross-sectional area, and development within a particular storm can be associated with other storm-based properties such as storm evolution, hail production, and tornadic potential (e.g.,

Kuster et al. 2019; French and Kingfield 2021; Segall et al. 2022).

The operational utility of Z_{DR} columns in observations collected by the WSR-88D network has been limited by poor vertical resolution due to scanning strategies that prioritize low-level scans over midlevel scans (e.g., Kingfield and French 2022; Cho et al. 2022). Because of this, Z_{DR} column detection techniques like the one proposed by Snyder et al. (2015; hereafter referred to as S15) lack consistency when the Z_{DR} column is in a region of the domain with poor vertical sampling or coverage (which is common at ranges > 100 km). Additionally, the WSR-88D network experiences a Z_{DR} bias of $>\pm0.2$ dB on about 20% of its radars at any given time (D. Zittel 2023, personal communication). Such a bias can create errors in Z_{DR} column detection and the determination of its depth when a fixed threshold (e.g., $Z_{DR} \geq 1$ dB) is used. The high values of Z_{DR} produced in the melting layer as snow melts into rain can also create errors (false positives) in other Z_{DR} column identification methods such as the Thunderstorm Risk Estimation from Nowcasting Development via Size Sorting (TRENDSS) algorithm (Kingfield and Picca 2018; French and Kingfield 2021). The TBSS (three-body scatter signature; Zrnić 1987) described by Lemon (1998) is an artifact in the radar data that produces both high Z_{DR} and low-to-moderate Z. This artifact is often found adjacent to strong storms and near true Z_{DR} columns and can be a challenge for all Z_{DR} column detection algorithms.

Our proposed Z_{DR} column detection method, the hotspot technique, seeks to identify the base of the Z_{DR} column on a single level rather than throughout its entire vertical extent. Identifying the base of the Z_{DR} column on a single level (e.g.,

---

🖉 Supplemental information related to this paper is available at the Journals Online website: https://doi.org/10.1175/WAF-D-23-0146.s1.
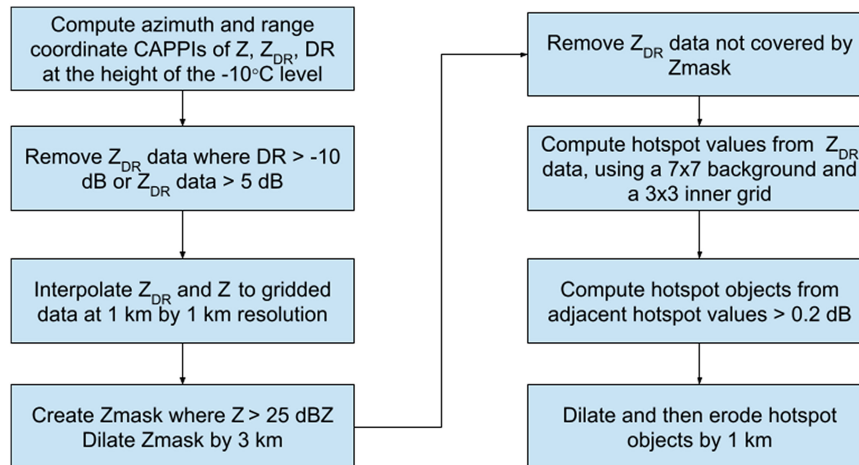
Corresponding author: John Krause, John.Krause@noaa.gov

FIG. 1. A flowchart summarizing the computational steps of the Z_{DR} hotspot technique.

the −10°C CAPPI) is easier than previous efforts (i.e., S15 and TRENDSS), which try to locate Z_{DR} columns using data from multiple elevation angles. Our Z_{DR} hotspot technique can assist forecasters in identifying a storm's updraft location and assessing that storm's strength, structure, and whether it is growing or decaying (e.g., Kuster et al. 2020). The Z_{DR} hotspot technique identifies areas in the data where the local median of Z_{DR} is greater than the median of the surrounding data. Due to this local data-to-data comparison, the technique is both Z_{DR} calibration independent and applicable to radar variables other than Z_{DR}. Confidence in the identified Z_{DR} hotspot being related to a storm's updraft is increased by being near a strong VIL (vertically integrated liquid) or reflectivity (Z) maximum. Although beyond the scope of this paper, the method could also be applied to correlation coefficient (ρ_{hv}), K_{DP}, azimuthal shear, or other radar fields; for example, if looking for large and giant hail, it can also be used to identify negative Z_{DR} anomalies (e.g., Kumjian et al. 2010; Witt et al. 2018).

2. Algorithm description

This hotspot technique (Fig. 1) begins by computing azimuth and range coordinate CAPPIs of Z_{DR}, Z, and a circular depolarization ratio proxy (Ryzhkov et al. 2017) at the height of the −10°C isotherm (Figs. 2a–c). Depolarization ratio (DR) is a combination of Z_{DR} and ρ_{hv} that serves as a proxy for circular depolarization ratio (CDR), which contains information about scatterers' shape and water (ice) phase composition. Hailstones, wet snowflakes, TBSS, and nonmeteorological scatterers are characterized by large values of DR (i.e., from −15 to 0 dB). We chose to remove the Z_{DR} data where DR > −10 dB. This DR threshold value specifically aims to remove any TBSS and is less restrictive than the −12-dB threshold originally proposed in Kilambi et al. (2018), which targets all nonmeteorological data. Figure 2d shows the locations of DR > −10 dB in orange, which correspond to small TBSS detections. The CAPPI height is set to the height of the −10°C isotherm (see discussion below) and is constant throughout the domain. It can be obtained from

a model data vertical profile or sounding near the radar of interest. In our experience, −10°C is the lowest height where reliable detection of the Z_{DR} column signature can be expected, without contamination by the melting layer. Locations with Z_{DR} > 5 dB, which are not commonly found in meteorological data at S band even when large drops are present (although the biggest raindrops, e.g., those exceeding 7 mm in diameter, may be associated with such high Z_{DR}), are then removed. We interpolate the Z and trimmed Z_{DR} data from azimuth and range coordinates to a 1-km grid with a 5 data-point average of the radial data, using the nearest radial point to the target grid point (nearest neighbor) and the surrounding radial points in both azimuth and range (5 gate arithmetic average; Langston et al. 2007; Fig. 2e).

Finally, to focus our method on convection, we create a Z mask from gridded Z data on a CAPPI, identifying all locations where Z > 25 dBZ. We dilate this mask by 3 km in each (i.e., x and y) direction, enlarging the detection region and filling gaps (Fig. 2c). The Z mask is applied to the Z_{DR} data such that all Z_{DR} data not covered by the mask are removed. All of the above works to limit the technique's detection to locations with meteorological data near convective storms at the height of the −10°C isotherm.

To create the Z_{DR} hotspot field using our trimmed Z_{DR} data (Fig. 2e), for each grid point we compute the 3 × 3 gridded (9 km²) local median and the surrounding 7 × 7 background median; the 9 gates of the 3 × 3 local area are *not included* in the median of the 40 gates from the surrounding 7 × 7 background area, so the surrounding median covers 40 km² (Fig. 3). The value of the Z_{DR} hotspot is the difference between the local area median and the background area median:

$$Z_{DR} \text{ hotspot value} = \text{local area } Z_{DR} \text{ median } (9 \text{ km}^2)$$
$$- \text{ background area } Z_{DR} \text{ median } (40 \text{ km}^2).$$

Now that the field of Z_{DR} hotspots is available, we can highlight those locations in the field that exceed 0.2 dB for further review. We selected the value of 0.2 dB as our threshold
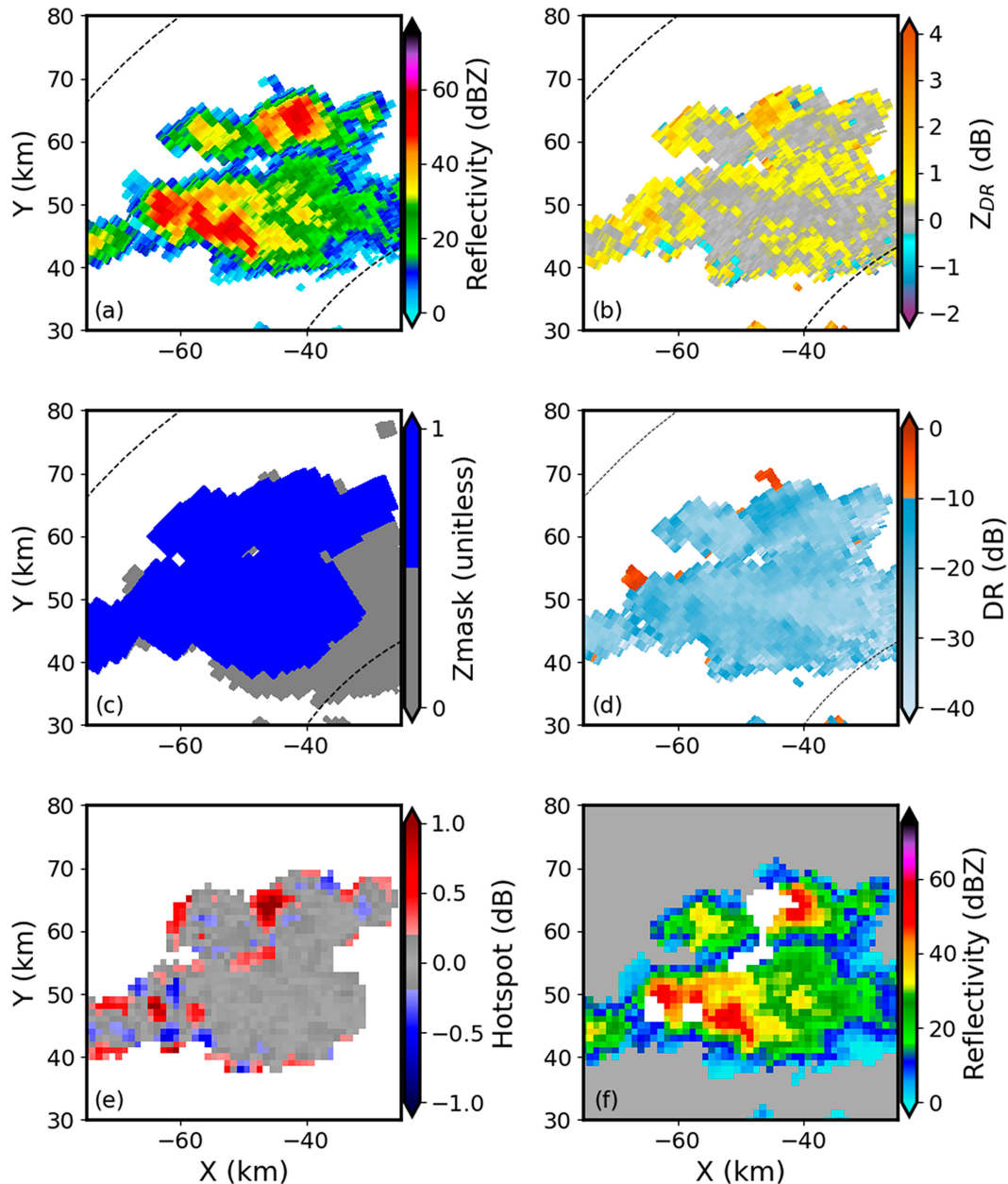
FIG. 2. (a) Z_H (reflectivity), (b) Z_{DR}, (c) Z mask (blue) overlaid on reflectivity (gray), (d) DR, (e) Z_{DR} hotspots, and (f) Z_{DR} hotspot objects (white) overlaid on gridded reflectivity. All CAPPI data are from 2057 UTC 12 Jun 2014 at KDYX (Dyess Air Force Base, TX) at the height of the $-10°$C temperature level (5.83 km AGL).

because this value would capture almost all points greater than one standard deviation above the mean hotspot value over multiple cases. A list of the cases used to develop the hotspot technique and the number of volumes for each case is listed in Table 1. A histogram of the hotspot values for the KOAX (Omaha, Nebraska) case on 3 June 2014 can be found in Fig. S1 of the online supplemental material and shows the new variable to be normally distributed.

Adjacent points that exceed the 0.2-dB threshold are grouped together and identified as an object. Objects with an area of <5 km^2 are removed to reduce the number of objects and to keep only those objects that are likely to exist at the next time step. Each object is required to have at least one point with $Z > 20$ dBZ. Objects then undergo a dilatation and erosion procedure that combines objects separated by 2 km or less. Dilation and erosion are morphological image procession operations. In this case, the dilation procedure adds any pixel within 1 km of an object pixel to the object and then the erosion procedure removes any pixel of the object that is within 1 km of the edge of the object. Once the dilation
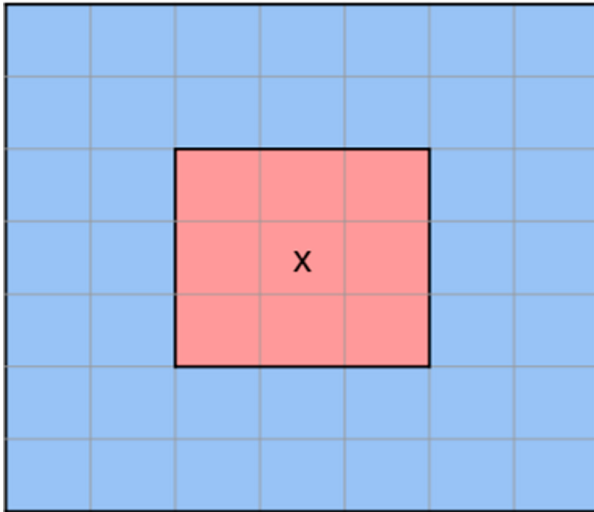
FIG. 3. The hotspot method computed for the location "X" is the difference between the median of the data in the salmon-colored inner box (9 km^2) and the median of the data in the light blue colored data (40 km^2). Each box outlined by the light gray and/or black lines is 1 km^2.

and erosion processes are complete, the remaining objects are now considered probable updrafts (Fig. 2f).

Now that we have described the hotspot method, it is important to examine the selection of both the height at which we compute the hotspot (i.e., the height of the −10°C isotherm) and the size of the grids used to compute the value of the hotspot itself [7 × 7 background grid (outer) and 3 × 3 inner grid]. Figure 4 shows the hotspot method results for four different sized grids. The hotspot data for Figs. 4 and 5 has been converted into its standard deviation (σ level), where the values of standard deviation greater than 1.0 are colored in red and values less than −1.0 are colored in blue. The conversion into standard deviation allows for a fair comparison between the results from the different grid sizes because the standard deviation of the largest grid (11 × 11, Fig. 4f) is much smaller than the standard deviation of the smallest grid (5 × 5, Fig. 4c). Finally, a standard

deviation of >1.0 or <−1.0 suggests a location where the value of the hotspot data is of interest.

Figure 4 is presented at a scale of 150 km × 150 km so that the reader can evaluate the character of the hotspot method in general. The smallest background grid (5 × 5; Fig. 4c) shows significantly more and separate hotspots (indicated in red) that are smaller in size than that of the largest background grid (11 × 11; Fig. 4f). The inset black box in Fig. 4a shows the location of Fig. 5, where a more detailed view is presented.

Figure 5 shows small, medium, and large hotspots denoted with green, cyan (light blue), and yellow arrows, respectively. The smaller hotspot identified by the green arrow has been broken into two different areas on the smallest background grid (5 × 5; Fig. 5c), but because the signal in the Z_{DR} data is weak, this hotspot is not identified in the 11 × 11 background grid (Fig. 5f). The hotspot location pointed to by the cyan arrow is identified on all grids, but we find that the 7 × 7 background grid (Fig. 5d) does the best job of grouping large adjacent hotspot values and identifying the areal extent of the hotspot. Finally, for the largest hotspot (yellow), we note that for the smallest scale (5 × 5; Fig. 5c), the maximum values of the hotspot are not adjacent, and that the areal extent of the hotspot decreases as the background grids increase in size. Our analysis finds that the 7 × 7 background grid with a 3 × 3 inner grid (Fig. 5d) is the best performing combination for Z_{DR} data.

When we selected the height at which to run the hotspot method (−10°C) we considered a number of factors. It is our hypothesis that high Z_{DR} values found above the environmental freezing level are large raindrops or wet hail held aloft by strong convective updrafts. The creation of CAPPIs near 0°C can contain high Z_{DR} values created by melting snow rather than lofted large drops or wet hail. However, weak convective updrafts may not reach much beyond the height of the environmental freezing level. Figure 6 shows the performance of the hotspot method for different heights using the preferred 7 × 7 background grid and 3 × 3 inner grid.

The hotspot CAPPI at 0°C (Fig. 6c) contains numerous hotspots, while the −10°C panel (Fig. 6d) shows a more reasonable number compared to the number of storm cells in the reflectivity data (Fig. 6a). Both the −20°C (Fig. 6e) and

TABLE 1. Data used to develop the hotspot algorithm (STD = standard deviation).

| Radar ID	Start date	Start time (UTC)	No. of volumes	Avg hotspot value (dB)	STD of hotspot values (dB)
KDGX	25 May 2023	0000	29	−0.0012	0.1896
KDYX	12 Jun 2014	1800	116	0.0304	0.2361
KEWX	4 May 2021	0000	57	0.0121	0.2976
KFDR	22 May 2020	2100	90	0.0134	0.2137
KFWS	12 Apr 2016	0000	83	0.0188	0.2350
KFWS	24 Mar 2019	2100	93	0.0551	0.2742
KICT	24 Jul 2013	0000	98	0.0323	0.2618
KOAX	3 Jun 2014	1800	119	0.0100	0.2059
KSJT	12 Jun 2014	2000	109	0.0295	0.2338
KTLX	27 Feb 2023	0000	66	0.0136	0.2239
KUDX	19 Jun 2015	2300	86	0.0075	0.1810
			Total volumes	Avg	Avg STD
			946	0.0201	0.2321
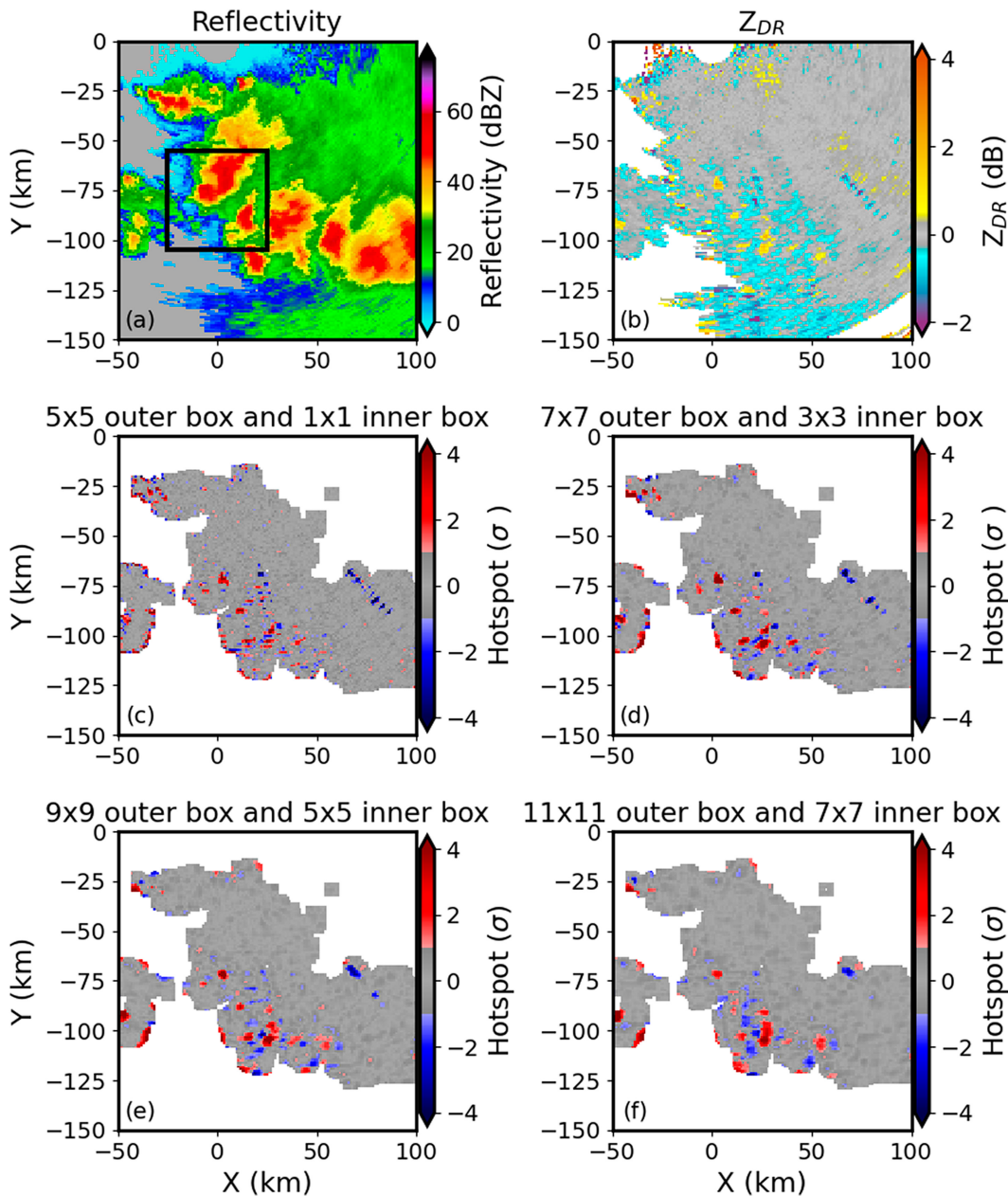
FIG. 4. (a) Reflectivity, (b) Z_{DR}, and Z_{DR} hotspots (in σ levels) for a (c) 5×5 outer box, (d) 7×7 outer box, (e) 9×9 outer box, and (f) 11×11 outer box. All data are from 0358 UTC 23 May 2020 at KFDR at the height of the $-10°$C isotherm (5.547 km AGL) The inset black box in (a) is the region shown in Fig. 5.

$-30°$C (Fig. 6f) hotspot fields show a distinct lack of hotspot detections, as only the strongest storms can loft large drops and wet hail to these heights.

3. Results and discussion

a. Results and limitations of the hotspot technique

Results of the hotspot technique are demonstrated in Figs. 7 and 8 where hotspots are computed for a set of severe storms along the Oklahoma/Texas border on 24 March 2019 as viewed by KFDR (Frederick, Oklahoma). The updrafts of these storms have been identified by the technique and are located adjacent to large areas of higher Z. Compared to the Z_{DR} output in Fig. 7b, the hotspot field (Fig. 7c) clarifies the locations of the updrafts, and overlaying all hotspot locations > 0.2 dB as white on the Z image (Fig. 7d) demonstrates the presence of Z_{DR} hotspots at plausible updraft locations.

Figure 8 is a zoomed in view of one of the larger and more complex storm cells shown in Fig. 7. A bounded weak echo
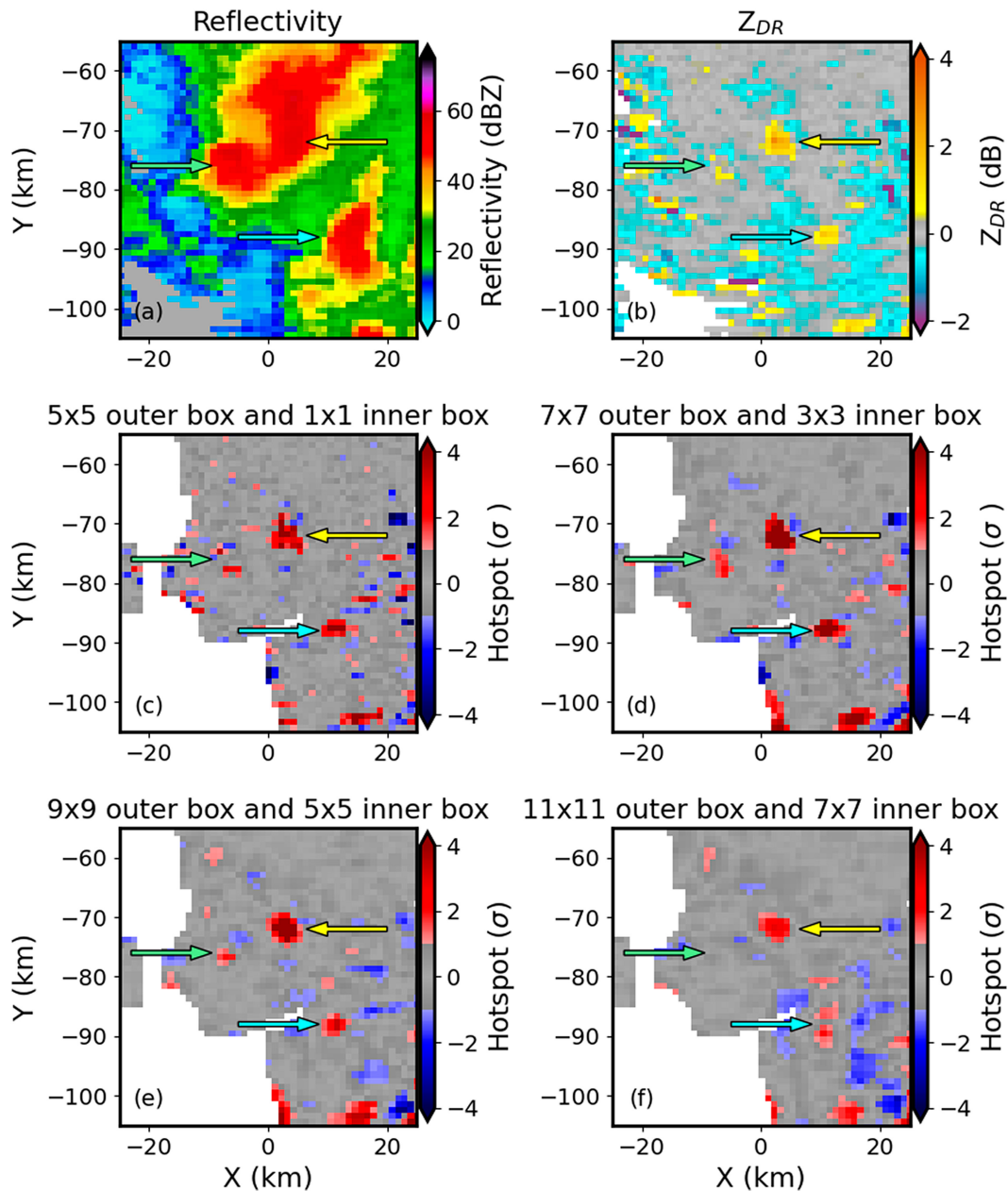
FIG. 5. As in Fig. 4, but for the subsetted area shown in Fig. 4a. The green, yellow, and cyan arrows identify hotspots of different sizes.

region (BWER) (verified by examining multiple elevations not shown) is visible in Fig. 8a at $x = -25$ km and $y = -68$ km, which suggests a strong updraft is present. The Z_{DR} data in Fig. 8b has a number of points where Z_{DR} is >1 dB, suggesting drop size sorting collocated with an updraft and also $Z_{DR} < -1.0$ dB, suggesting possible large hail. Finally, a region runs from the upper-right corner ($x = -20$ km, $y = -50$ km) to the lower-left corner ($x = -40$ km, $y = -85$ km) of Fig. 8b, where all of the Z_{DR} values are lowered, suggesting differential attenuation due to a storm closer to the radar and/or from parts of the storm shown. The Z_{DR} hotspot technique

(Fig. 8c) identifies three large areas with values > 0.2 dB and several smaller ones with areas less than 5 km^2. The effects of removing the smaller detections and the dilate and erode procedure are evident in the white spots overlaid on the Z data in Fig. 8d. Only the three larger areas from Fig. 8c remain and those areas have been slightly filled by the dilate and erode procedure. The larger cells were just far enough apart that they were not combined. Overall, the remaining hotspots show two cells associated with the BWER and another cell forming along the southwest edge of the storm. One of the primary benefits of the hotspot technique is the identification
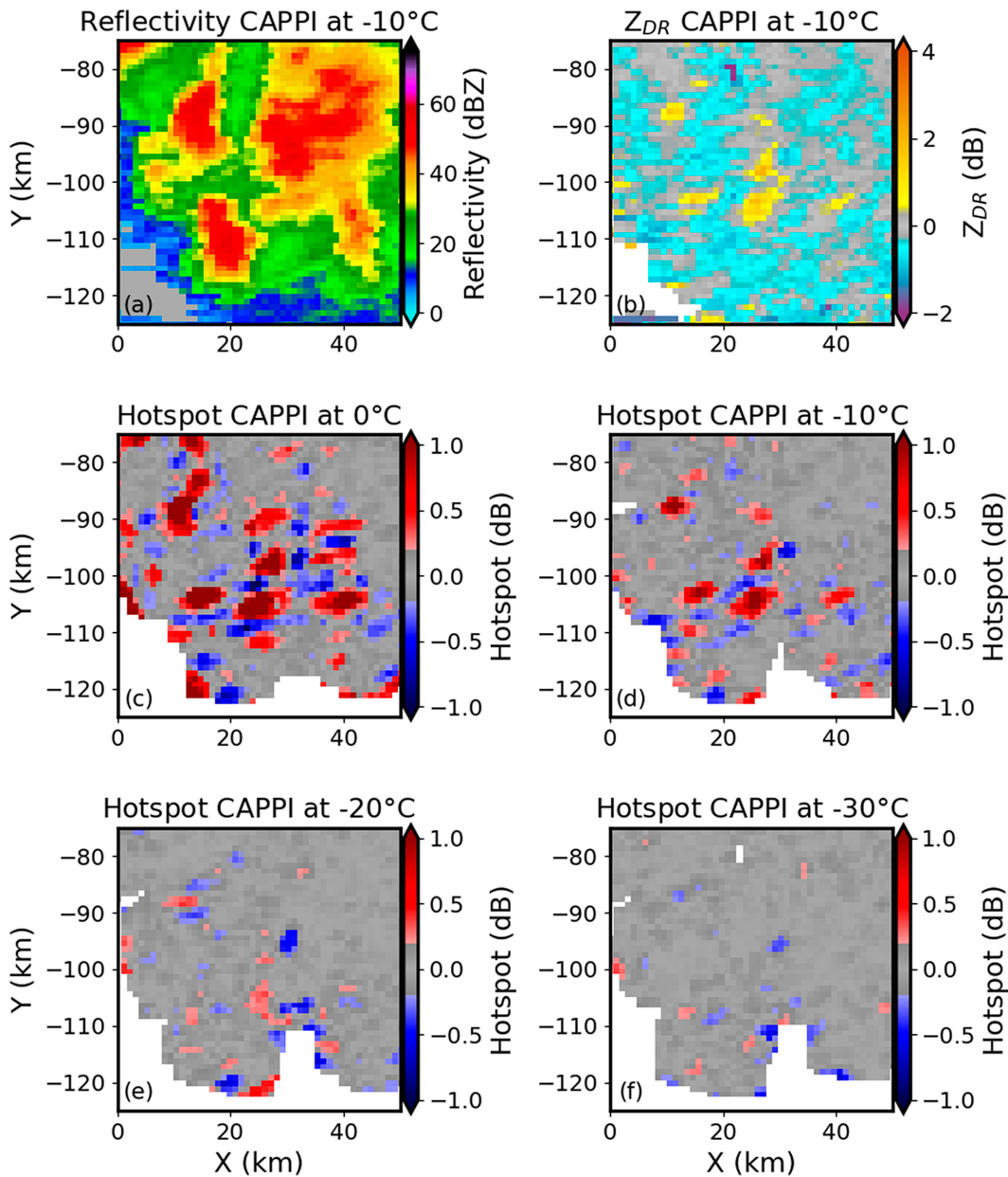
FIG. 6. (a) Reflectivity at $-10°C$, (b) Z_{DR} at $-10°C$, and Z_{DR} hotspots at the heights of the (c) 0°, (d) $-10°$, (e) $-20°$, and (f) $-30°C$ isotherms. All data are from 0358 UTC 23 May 2020 at KFDR with a 7×7 background grid and a 3×3 inner grid.

of newly formed convection, such as the cell on the southwestern edge ($x = -30$ km, $y = -80$ km).

Figure 9 illustrates an error we observed on multiple occasions. The data are from KEWX (New Braunfels, Texas) at 0010 UTC 4 May 2021 and show three strong storms located from north to south. There is a consistent ribbon of high Z_{DR} that forms along the western edge of each updraft (yellow colors in Fig. 9b) and down radial from the radar. In the northern storm there is a TBSS evident, which might be one explanation for this region of high

Z_{DR}, but the other two storms do not show evidence of a TBSS and yet contain the elevated Z_{DR} along the edge of the storm. The hotspot technique identifies this edge region of high Z_{DR} (Fig. 9, pink arrows) and combines it with nearby updrafts (Fig. 9, yellow arrows) in error. Updrafts embedded in surrounding precipitation do not experience this kind of error. Data sampled with a low signal-to-noise ratio, oblate ice crystals, and TBSS are all possible explanations of this high Z_{DR} data; regardless, the hotspot technique misidentifies these areas as an updraft region.
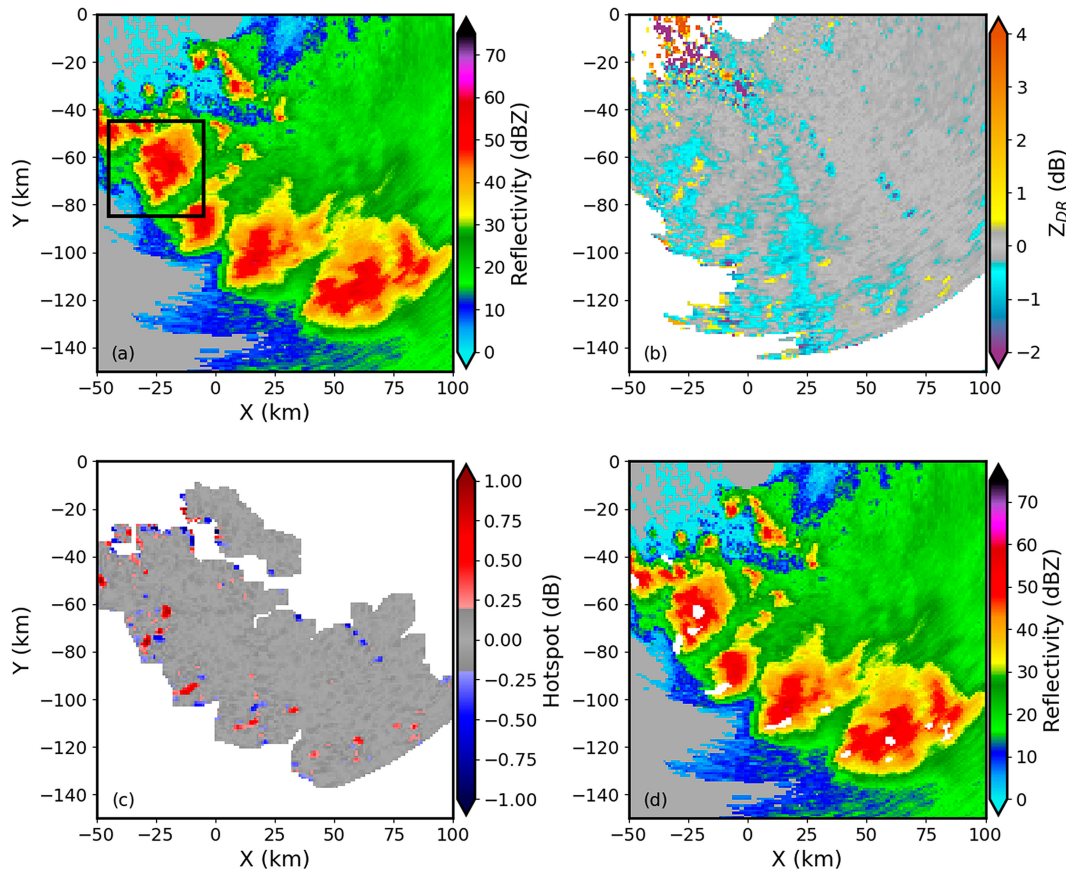
FIG. 7. (a) Reflectivity, (b) Z_{DR}, (c) Z_{DR} hotspot, and (d) Z_{DR} hotspot objects (white) overlaid on reflectivity. All data from 0457 UTC 23 May 2020 at KFDR at the height of the $-10°C$ isotherm (5.547 km AGL). The inset black box in (a) shows the region shown in Fig. 8.

The technique may also encounter difficulties when applied in regions with poor data quality. Figure 10 shows an example of this in an area located just beyond the maximum unambiguous range. We note that other methods for Z_{DR} column identification (e.g., TRENDSS, S15) also tend to struggle in regions with poor data quality. In this example, the area located just beyond the maximum unambiguous range ($\sim$160 km) impacts the algorithm by producing noisy Z_{DR} values and several false updraft detections (Fig. 10). The detections inside the black box can be identified as false because they occur away from strong signatures (e.g., $Z > 45$ dBZ). The algorithm is usually reliable within the maximum unambiguous range and can be extended to distances beyond it if the poor data quality of the transition zone between the maximum unambiguous range and the unfolded region is taken into account. In our experience the technique produces usable data for storms located $<$200 km from the radar. At far ranges (i.e., $>$200 km), the lowest elevation collected by the radar may rise above the height of the $-10°C$ isotherm, although this is uncommon in convective environments where the height of the $-10°C$ isotherm almost always exceeds 2 km. At longer ranges, other factors can reduce the

reliability of the technique, such as the size of the beam relative to the size of the updraft, the interpolation of radial data to gridded Cartesian data, and the conversion of data into CAPPI outputs where one elevation may be in the melting layer, or where only one elevation may be used.

The data from KOAX at 0102 UTC 4 June 2014 (Fig. 11) is a complex case with multiple storms in the domain that would require analysis by forecasters. In the center of the image there are two separate storms, each with a developing flanking line. The hotspot technique identifies the updrafts of both the parent storm and storms developing along the flanking line. Forecasters who want to interrogate the data to determine storm strength and issue warnings can quickly find each storm updraft using the results from the hotspot technique.

During our testing and evaluation we noticed strong supercells for which the Z_{DR} hotspot object would either become too small (i.e., below the $<$5-km^2 detection threshold) or disappear entirely. This lack of detection occurred despite obvious markers of storm strength such as $Z_H > 50$ dBZ at the height of the $-10°C$ isotherm. We illustrate this using an example from 0211 UTC 4 May 2021 (Fig. 12), in
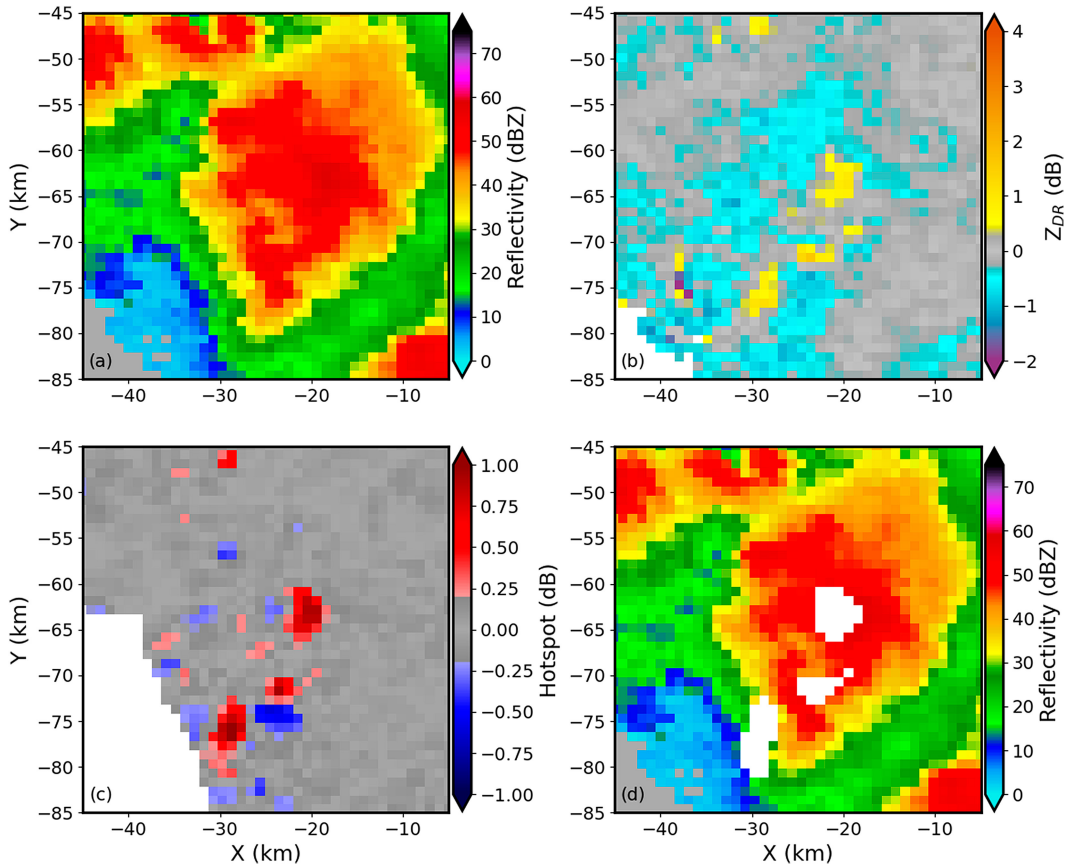
FIG. 8. As in Fig. 7, but for the subsetted area shown in Fig. 7a.

which the Z_{DR} hotspot became smaller than 5 km^2 (shown by the yellow arrow in Figs. 12a,c). In this case, we also noticed that raw Z_{DR} values (Fig. 12b) were lower than the Z_{DR} from the previous scan (not shown). Evidence of large hail is suggested by an area of low correlation coefficient (CC) where the updraft would be expected to be located (as subjectively assessed using radar training and knowledge of convective storm structure) and a significant TBSS (Fig. 12a, pink arrow). We suspect that the previously observed strongly positive Z_{DR} values of large liquid water drops are being reduced by the strong $Z_{\mathrm{DR}} \sim 0$ dB contribution of hail, possibly large, inside the updraft (e.g., Kumjian et al. 2014). The disappearance of a Z_{DR} hotspot for a mature cell could be an indicator of falling hail.

b. Comparison with existing updraft detection methods

The Z_{DR} hotspot technique was compared to both the S15 method and TRENDSS (Kingfield and Picca 2018). In the S15 method, it is assumed that any quality controlled Z_{DR} value > 1 dB that is located at and above the height of the 0°C level is due to size sorting in convective updrafts. As such, the output of the S15 algorithm is not a location where size sorting is taking place but rather a Z_{DR} column depth computed by identifying vertically adjacent Z_{DR} values > 1 dB in a volume of data. A common

deficiency of the S15 method is its dependence on a constant and arbitrary Z_{DR} threshold of 1 dB. As such, the method can over detect the presence of Z_{DR} columns due to high Z_{DR} bias, or under detect due to low Z_{DR} bias. In practice, however, it is difficult to get consistent results from S15; unreliable detections of Z_{DR} column depth can be created from volume scan strategies that create large vertical gaps in the data and volume samples that are spaced far apart in time (>5 min), tilted or fast-moving storms, TBSS, and areas of poor data quality like those just beyond the maximum unambiguous range. Both the TRENDSS method and the Z_{DR} hotspot technique can produce Z_{DR} column depths like those in S15 by applying the method to vertically adjacent data, but the same problems that produce inconsistent results for S15 exist in these approaches.

The TRENDSS method first described in Kingfield and Picca (2018), and then modified by French and Kingfield (2021), was developed to identify drop size sorting in radar data. The method creates histograms of quality-controlled Z_{DR} for each 5-dBZ range of Z between 15 and 60 dBZ (e.g., 15–20, 20–25 dBZ, etc.). These histograms of Z–Z_{DR} are created for three different levels: below the melting layer, within the melting layer, and above the melting layer. The standard deviation of Z_{DR} is then calculated
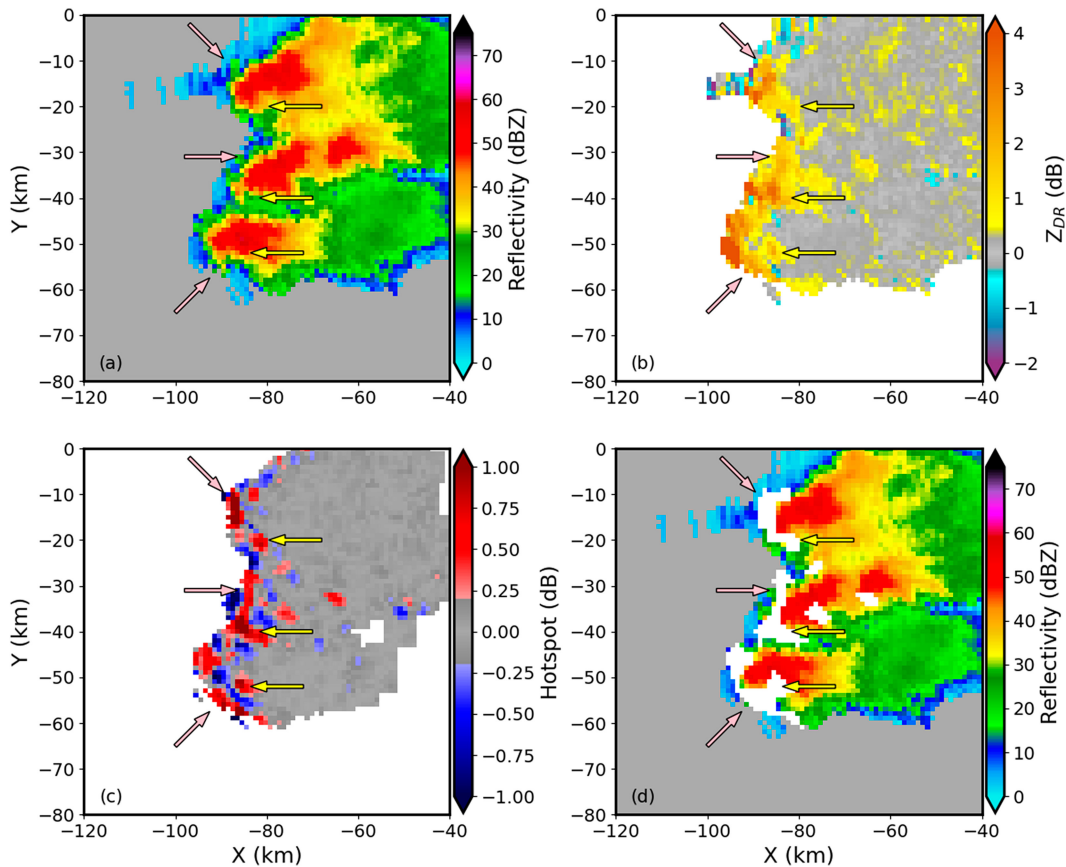
FIG. 9. (a) Reflectivity, (b) Z_{DR}, (c) Z_{DR} hotspots, and (d) Z_{DR} hotspot objects (white) overlaid on reflectivity. All data from 0010 UTC 4 May 2021 at KEWX at the height of the $-10°C$ isotherm (5.501 km AGL). False detections of updraft regions are identified by pink arrows, and the true updraft regions are identified by the yellow arrows.

for each Z range at each level. Size sorting locations are identified by computing the standard deviation (σ level) of Z_{DR} at each location relative to the computed Z–Z_{DR} histogram at the appropriate height and Z level. Because the TRENDSS method uses σ as a measure of size sorting it can be directly compared to the Z_{DR} hotspot technique once the σ of the Z_{DR} hotspot values has been computed.

To create a fair comparison, we modified the TRENDSS method so that it runs on the trimmed Z_{DR} data from the $-10°C$ CAPPI. We then computed the standard deviation of the hotspot data (σ level) as a comparator to the TRENDSS output. Figure 13 compares the three methods for multicellular storms on 23 May 2020 viewed by the KFDR radar. For the group of storms shown, we note that all three methods' maximum values are located in roughly the same place. Also located in this image is an area of data with reduced Z_{DR}, identified by the yellow box. A strong storm located close to the radar has caused differential attenuation. This is a very common local phenomenon that reduces Z_{DR} for typically a small number of radials in the volume. Because the S15 algorithm uses a static 1-dB

threshold, Z_{DR} in this region has been reduced enough that the lowest level does not contribute to the Z_{DR} column height computation. As a result, S15 Z_{DR} column heights at this location are about 1 km lower than nearby Z_{DR} columns. The output from TRENDSS is also affected by the differential attenuation because the Z_{DR} mean and σ values used in TRENDSS are computed from all of the data in the CAPPI. Therefore, the TRENDSS data show a strong negative Z_{DR} bias in this region (blue). The Z_{DR} hotspot method, however, is relatively unaffected by this problem due to its reliance on data near the analysis location.

Another comparison between the three Z_{DR} column methods is presented in Fig. 14. In data from 4 June 2014 at KOAX, the Z_{DR} field has a positive bias of about 0.42 dB, as determined by computing the average value of Z_{DR} in dry snow (Richardson et al. 2017). This bias creates a significant overdetection of Z_{DR} columns by S15 as shown in Fig. 14f. The over detection of updraft locations by the TRENDSS output (Fig. 14d) is more difficult to explain. We suspect that there are problems in the creation of the Z–Z_{DR} relationships that underpin the algorithm.
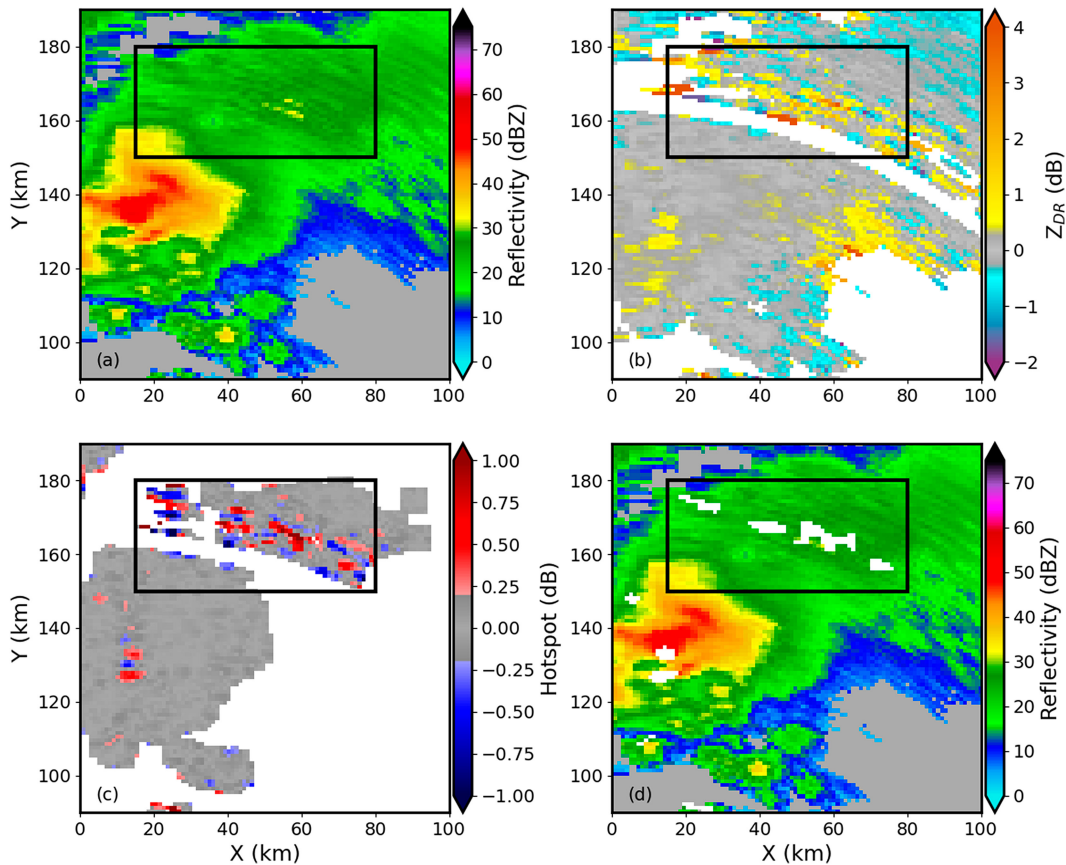
FIG. 10. As in Fig. 9, but for 0224 UTC 25 Mar 2023 at KDGX (Jackson, MS) at the height of the $-10°$C isotherm (5.488 km AGL). An area with multiple false detections is indicated by the black box.

Much of the domain, not shown in the image, contains meteorological data in both Z and Z_{DR} at the height of $-10°$C. The creation of Z–Z_{DR} histograms for this radar at this time at this height could be dominated by ice particles with low and relatively homogeneous Z_{DR} values. Such particles would have a much lower standard deviation of Z_{DR} than liquid drops. Therefore, when the TRENDSS algorithm computes the σ level of the Z_{DR} in locations where liquid drops are present it is always >1.0 (or higher) and as such it may not correspond to size-sorted drops in updraft locations but any type of liquid water or water-coated melting snow with enhanced Z_{DR} values. The Z_{DR} biases present in the data do not seem to affect the hotspot technique (Fig. 14d), which shows good separation between hotspots and multiple updrafts.

c. Temporal evolution of updraft objects

Several animations of data were created to demonstrate the Z_{DR} hotspot techniques' performance over time. They can be found in the supplemental material. In the first animation, Fig. S2 (KEWX, 1 h 40 min, 20 volumes), we revisit the KEWX case shown in Fig. 9. The detection errors along the edge of the storm echo in this case exist for the first 5–7 time steps ($\sim$30 min), but they are not found once

the storm is well organized. By the end of the animation the Z_{DR} hotspot technique shows a coherent updraft located on the southwest side of the storm. There are no edge errors in the later outputs even though there is a TBSS present in the data from 0129 UTC onward. Our experience suggests that the issues described in Fig. 9 and present early in Fig. S2 are generally found downradial of newly developed convection.

A much longer animation, Fig. S3 (KFDR, 4 h, 48 volumes), was created for a complex case with numerous hotspot detections present in the volume. This animation begins with a single supercell thunderstorm and then evolves into a multicellular storm. The Z_{DR} hotspot technique identifies the initial updraft and the animation shows this updraft's evolution over time. The consistency of the detection improves our confidence in the output of the algorithm. Later in the animation (after 0147 UTC), a multitude of smaller and more short-lived updrafts form and move throughout the domain. Although we have focused on the location of Z_{DR} hotspots > 0.2 dB as locations of interest, groups of particularly large values (>0.6 dB, approximately 3σ) in our experience suggest a well-organized updraft that forecasters would want to evaluate in more detail.
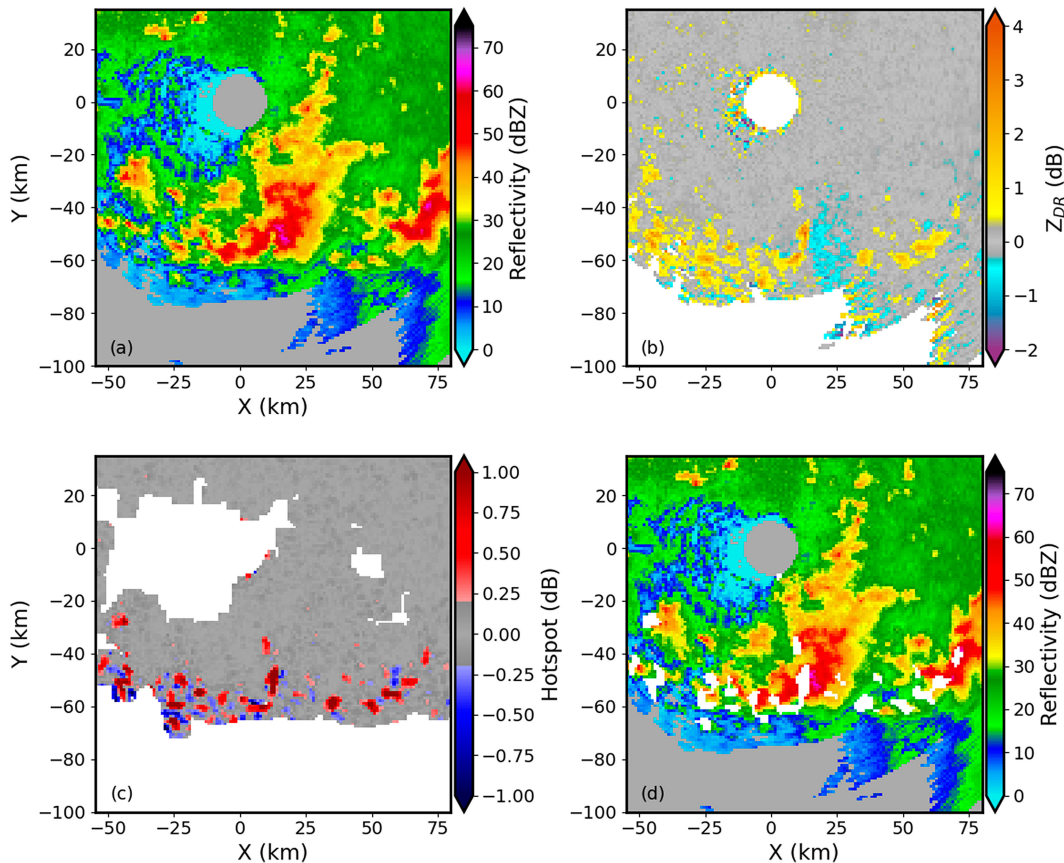
Fig. 11. As in Fig. 9, but for 0102 UTC 4 Jun 2014 at KOAX at the height of the $-10°\text{C}$ isotherm (5.188 km AGL).

Last, we created an animation of a linear system shown in Fig. S4 (KOAX, 2 h, 22 volumes). The hotspot technique identifies the high Z_{DR} values along the leading edge of the linear convective system as updraft locations. The edge effects identified in the first animation (Fig. S2) do not seem to be present in this event. As with the previous example, the location of the Z_{DR} hotspots with very large values (>0.6 dB) can be used to identify the stronger cells in the linear system.

4. Summary and future work

In this paper we have described and demonstrated the new Z_{DR} hotspot technique, which identifies the base of Z_{DR} columns in the $-10°\text{C}$ CAPPI data using Z_{DR}, Z, and DR. We associated locations detected by the technique with liquid water drops that have been size sorted (retaining the large drops) by an updraft. Possible errors in the technique's updraft detection can be created by poor data quality or high Z_{DR} values of unknown origin located on the edge of storms near an updraft. A comparison between the Z_{DR} hotspot technique and two other Z_{DR} column detection methods was shown. The Z_{DR} hotspot technique produces improved performance for areas with differential

attenuation and when a Z_{DR} bias is present. Forecasters can use the Z_{DR} hotspot technique to identify updrafts in the domain and to investigate near them for hazards. In complex nowcasting scenarios when multiple updrafts are present and time is limited, forecasters can use this hotspot technique to triage and focus on locations where the Z_{DR} hotspot technique yields very large values (>0.6 dB or 3σ), which we suspect are an indication of a strong updraft in a well-organized storm.

In the future, the Z_{DR} hotspot technique could be utilized to study the evolution of storm updrafts over time, and the properties of the identified updraft areas, such as their size and the magnitude of the hotspot value, could be linked to the likelihood of storm hazards. In future studies, we aim to identify precursor signatures for large or giant hail, tornadoes, and downbursts using this approach. The hotspot technique can also be applied to other polarimetric variables such as ρ_{hv}, K_{DP}, and/or azimuthal shear, which could enable identification of hail cores, K_{DP} columns, and mesocyclones, respectively. Finally, the identification of updrafts might be used by the storm-scale modeling community for polarimetric radar data assimilation (e.g., Carlin et al. 2017) or to evaluate the output of convection-allowing models.
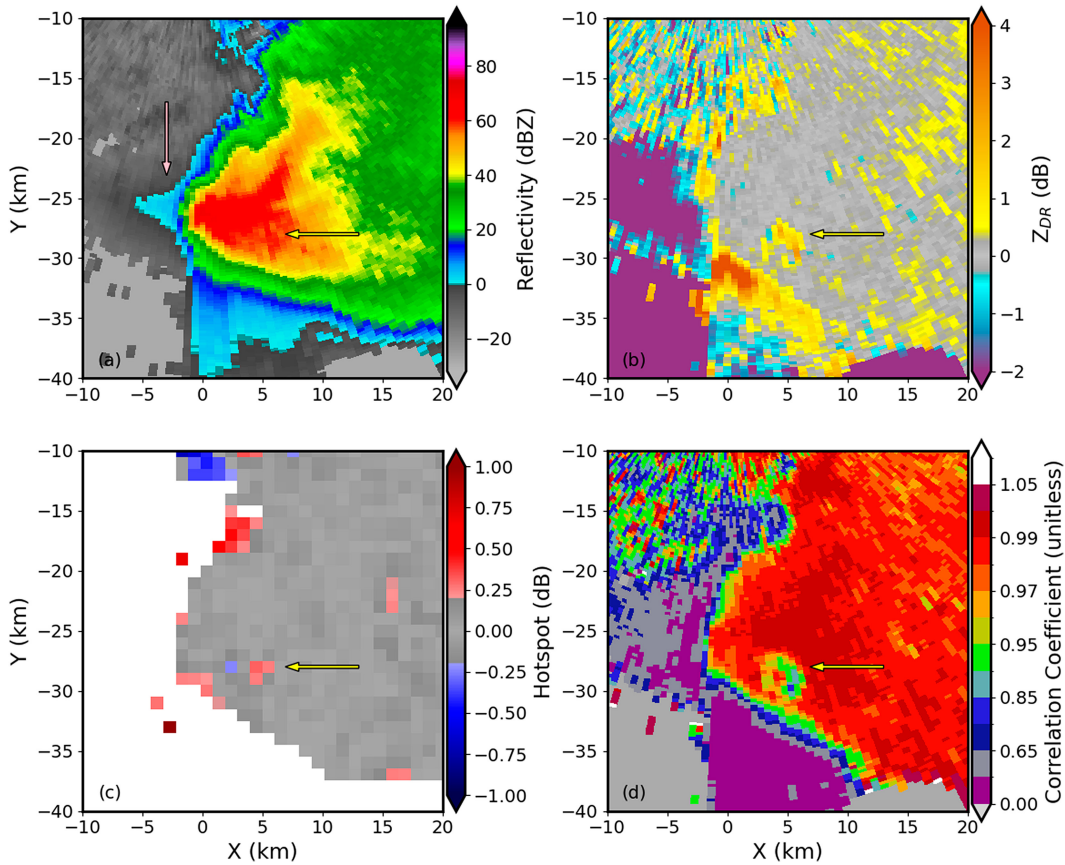
FIG. 12. (a) Reflectivity, (b) Z_{DR}, (c) Z_{DR} hotspot result, and (d) CC. All data from 0211 UTC 4 May 2021 at KEWX at the height of the −10°C isotherm (6.131 km AGL). The yellow arrow identifies the hotspot of interest.
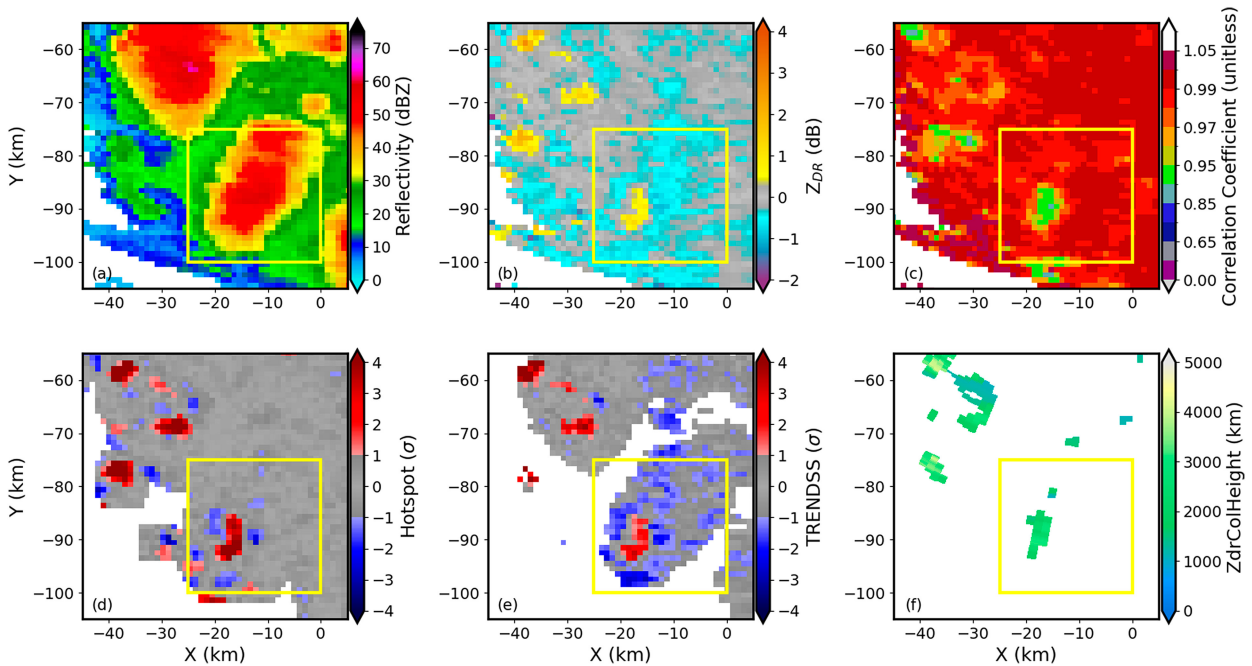

FIG. 13. (a) Reflectivity, (b) Z_{DR}, (c) CC, (d) Z_{DR} hotspot result, (e) TRENDSS result, and (f) S15 Z_{DR} column result. All data from 0447 UTC 23 May 2020 at KFDR at the height of the −10°C isotherm (5.547 km AGL).

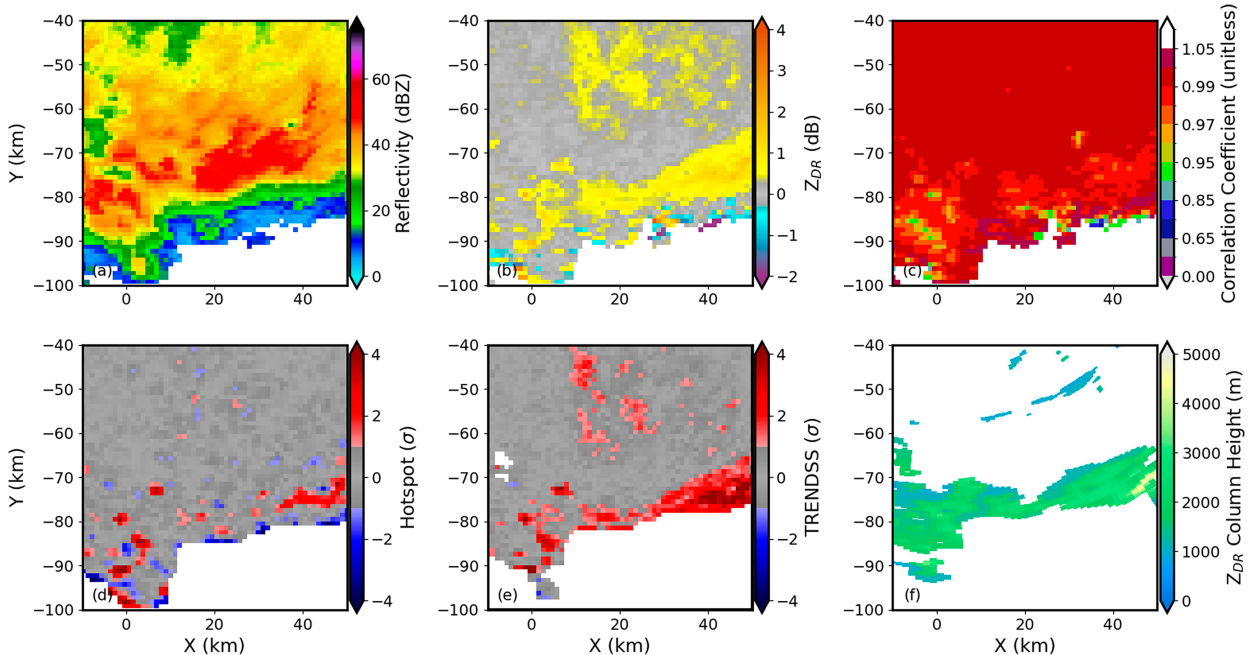FIG. 14. As in Fig. 13, but from 0455 UTC 4 Jun 2014 at KOAX at the height of the −10°C isotherm (5.188 km AGL).

Data availability statement. All radar data used in this study are publicly available from National Centers for Environmental Information (NCEI) at https://www.ncei.noaa.gov/products/radar.

REFERENCES

Carlin, J. T., J. Gao, J. C. Snyder, and A. V. Ryzhkov, 2017: Assimilation of Z_{DR} columns for improving the spinup and forecast of convective storms in storm-scale models: Proof-of-concept experiments. *Mon. Wea. Rev.*, **145**, 5033–5057, https://doi.org/10.1175/MWR-D-17-0103.1.

Cho, J. Y. N., J. M. Kurdzo, B. J. Bennett, M. E. Weber, J. W. Dellicarpini, A. Loconto, and H. Frank, 2022: Impact of WSR-88D intra-volume low-level scans on severe weather warning performance. *Wea. Forecasting*, **37**, 1169–1189, https://doi.org/10.1175/WAF-D-21-0152.1.

French, M. M., and D. M. Kingfield, 2021: Tornado formation and intensity prediction using polarimetric radar estimates of updraft area. *Wea. Forecasting*, **36**, 2211–2231, https://doi.org/10.1175/WAF-D-21-0087.1.

Kilambi, A., F. Fabry, and V. Meunier, 2018: A simple and effective method for separating meteorological from nonmeteorological targets using dual-polarization data. *J. Atmos. Oceanic Technol.*, **35**, 1415–1424, https://doi.org/10.1175/JTECH-D-17-0175.1.

Kingfield, D. M., and J. C. Picca, 2018: Development of an operational convective nowcasting algorithm using raindrop size sorting information from polarimetric radar data. *Wea. Forecasting*, **33**, 1477–1495, https://doi.org/10.1175/WAF-D-18-0025.1.

——, and M. M. French, 2022: The influence of WSR-88D intra-volume scanning strategies on thunderstorm observations and warnings in the dual-polarization radar era: 2011–20. *Wea. Forecasting*, **37**, 283–301, https://doi.org/10.1175/WAF-D-21-0127.1.

Kumjian, M. R., A. V. Ryzhkov, V. M. Melnikov, and T. J. Schuur, 2010: Rapid-scan super-resolution observations of a cyclic supercell with a dual-polarization WSR-88D. *Mon. Wea. Rev.*, **138**, 3762–3786, https://doi.org/10.1175/2010MWR3322.1.

——, A. P. Khain, N. Benmoshe, E. Ilotoviz, A. V. Ryzhkov, and V. T. J. Phillips, 2014: The anatomy and physics of Z_{DR} columns: Investigating a polarimetric radar signature with a spectral bin microphysical model. *J. Appl. Meteor. Climatol.*, **53**, 1820–1843, https://doi.org/10.1175/JAMC-D-13-0354.1.

Kuster, C. M., J. C. Snyder, T. J. Schuur, T. T. Lindley, P. L. Heinselman, J. C. Furtado, J. W. Brogden, and R. Toomey, 2019: Rapid-update radar observations of Z_{DR} column depth and its use in the warning decision process. *Wea. Forecasting*, **34**, 1173–1188, https://doi.org/10.1175/WAF-D-19-0024.1.

——, T. J. Schuur, T. T. Lindley, and J. C. Snyder, 2020: Using Z_{DR} columns in forecaster conceptual models and warning decision-making. *Wea. Forecasting*, **35**, 2507–2522, https://doi.org/10.1175/WAF-D-20-0083.1.

Langston, C., J. Zhang, and K. Howard, 2007: Four-dimensional dynamic radar mosaic. *J. Atmos. Oceanic Technol.*, **24**, 776–790, https://doi.org/10.1175/JTECH2001.1.

Lemon, L. R., 1998: The radar "Three-Body Scatter Spike": An operational large-hail signature. *Wea. Forecasting*, **13**, 327–340, https://doi.org/10.1175/1520-0434(1998)013<0327:TRTBSS>2.0.CO;2.

Richardson, L. M., W. D. Zittel, R. R. Lee, V. M. Melnikov, R. L. Ice, and J. G. Cunningham, 2017: Bragg scatter detection by the WSR-88D. Part II: Assessment of Z_{DR} bias estimation. *J. Atmos. Oceanic Technol.*, **34**, 479–493, https://doi.org/10.1175/JTECH-D-16-0031.1.

Ryzhkov, A. V., and D. S. Zrnić, 2019: *Radar Polarimetry for Weather Observations*. 1st ed. Springer, 486 pp.

——, and Coauthors, 2017: Estimation of depolarization ratio using weather radars with simultaneous transmission/reception. *J. Appl. Meteor. Climatol.*, **56**, 1797–1816, https://doi.org/10.1175/JAMC-D-16-0098.1.

Segall, J. H., M. M. French, D. M. Kingfield, S. D. Loeffler, and M. R. Kumjian, 2022: Storm-scale polarimetric radar signatures associated with tornado dissipation in supercells. *Wea. Forecasting*, **37**, 3–21, https://doi.org/10.1175/WAF-D-21-0067.1.

Snyder, J. C., A. V. Ryzhkov, M. R. Kumjian, A. P. Khain, and J. Picca, 2015: A Z_{DR} column detection algorithm to examine convective storm updrafts. *Wea. Forecasting*, **30**, 1819–1844, https://doi.org/10.1175/WAF-D-15-0068.1.

——, H. B. Bluestein, D. T. Dawson II, and Y. Jung, 2017a: Simulations of polarimetric, X-band radar signatures in supercells. Part I: Description of experiment and simulated ρ_{hv} rings. *J. Appl. Meteor. Climatol.*, **56**, 1977–1999, https://doi.org/10.1175/JAMC-D-16-0138.1.

——, ——, ——, and ——, 2017b: Simulations of polarimetric, X-band radar signatures in supercells. Part II: Z_{DR} columns and rings and K_{DP} columns. *J. Appl. Meteor. Climatol.*, **56**, 2001–2026, https://doi.org/10.1175/JAMC-D-16-0139.1.

Witt, A., D. W. Burgess, A. Seimon, J. T. Allen, J. C. Snyder, and H. B. Bluestein, 2018: Rapid-scan radar observations of an Oklahoma tornadic hailstorm producing giant hail. *Wea. Forecasting*, **33**, 1263–1282, https://doi.org/10.1175/WAF-D-18-0003.1.

Zrnić, D. S., 1987: Three-body scattering produces precipitation signature of special diagnostic value. *Radio Sci.*, **22**, 76–86, https://doi.org/10.1029/RS022i001p00076.